

Optical probing of phononic properties of a tin-vacancy color center in diamond

Cem Güney Torun,^{1,*} Joseph H. D. Munns,^{1,*} Franziska Marie Herrmann,¹ Viviana Villafane,^{2,3}
Kai Müller,³ Andreas Thies,⁴ Tommaso Pregnolato,^{1,4} Gregor Pieplow,¹ and Tim Schröder^{1,4,†}

¹*Department of Physics, Humboldt-Universität zu Berlin, 12489 Berlin, Germany*

²*Walter Schottky Institute, School of Natural Sciences and MCQST,
Technische Universität München, 85748 Garching, Germany*

³*Walter Schottky Institute, School of Computation, Information and Technology and MCQST,
Technische Universität München, 85748 Garching, Germany*

⁴*Ferdinand-Braun-Institut gGmbH, Leibniz-Institut für Höchstfrequenztechnik, 12489 Berlin, Germany*

The coherence characteristics of a tin-vacancy color center in diamond are investigated through optical means including coherent population trapping between the ground state orbital levels and linewidth broadening effects. Due to the large spin-orbit splitting of the orbital ground states, thermalization between the ground states occurs at rates that are impractical to measure directly. Here, spectral information is transformed into its conjugate variable time, providing picosecond resolution and revealing an orbital depolarization timescale of ~ 30 ps. Consequences of the investigated dynamics are then used to estimate spin dephasing times limited by thermal effects.

I. INTRODUCTION

In the last decade group-IV color centers in diamond (G4V), especially the silicon-vacancy (SiV), have emerged as a promising candidate for quantum technologies [1, 2]. The main advantage of this family of color centers stems from their inversion symmetric structure within the diamond lattice [3], that lends increased resistance to environmental charge noise (spectral diffusion) compared to the more widely studied nitrogen-vacancy color centers (NV) [4–6]. This advantage becomes particularly salient for integrated applications [7–10], where nanofabrication processes introduce surface charge noise in closer proximity to the color center.

Although the G4Vs have exceptional optical qualities, the two branched orbital ground states of the G4V energy manifold (Fig. 1(a)) allow spin-conserving phononic transitions and constitute the main decoherence channel for these quantum memories [11, 12]. In comparison, the NV is mainly protected from these thermal effects as the ground states have different spins and do not mix as quickly, enabling longer coherence times [13].

Among the G4Vs, the negatively charged tin-vacancy center in diamond (SnV), the third heaviest in the group-IV, has demonstrated better coherence properties at a given temperature [14] compared to lighter SiVs [15] and germanium-vacancy centers [16]. The heavier dopant atom results in a large ground state splitting ~ 830 GHz that is advantageous for the coherence properties of the spin states in the lower branch [11]. In particular, it allows coherence times not limited by phononic processes at cryogenic temperatures of few K [14, 17, 18] for the SnV spin, in contrast with the mK temperatures required by SiVs [19, 20]. Furthermore, although the Debye-

Waller factor is slightly reduced in comparison with the SiV ($\sim 60\%$ [21] instead of $\sim 70\%$ [22]), also as a consequence of the dopant size, higher quantum efficiency is expected due to reduced coupling to thermal processes [23].

These properties pinpoint SnVs as a favorable platform for integrated photonic quantum information processing [24, 25]. Understanding the decoherence dynamics of the SnV color centers, however, is imperative for developing more efficient techniques for coherent control. Therefore quantifying the phononic processes constitutes an important benchmark for the performance of G4V qubits.

In order to investigate these processes in the SnV, firstly, the linear (single-phonon) and cubic (two-phonon) linewidth broadening regimes are identified by monitoring the evolution of an optical transition linewidth as a function of temperature. Orbital depolarisation rates are then measured through conducting coherent population trapping (CPT) [18, 26–29]. Finally, from another broadened optical transition, the same process is independently analyzed and compared with the CPT measurements. All the experiments here are conducted on a sample with nanopillars which allow higher photon extraction efficiencies [30, 31].

II. ELECTRON-PHONON COUPLING

The SnV is a four-level system under zero-magnetic field (Fig. 1(a)), similar to other G4Vs [32]. It contains four orbital levels, two in the ground state manifold, and two in the excited. At cryogenic temperatures only two photonic relaxation channels are observable: conventionally named C transition between levels $|1\rangle$ and $|3\rangle$ (γ_C) and D transition between levels $|2\rangle$ and $|3\rangle$ (γ_D).

Decoherence mechanisms between the ground orbital levels of an SnV can be described in terms of relaxation between the two levels γ_{\pm} and pure dephasing γ_d

* These authors contributed equally to this work

† Corresponding author: tim.schroeder@physik.hu-berlin.de

(Fig. 1(a)). For the orbital levels, these processes are dominantly mediated by interactions with phonons, which includes direct single-phonon and Raman-like two-phonon transitions between the orbitals, as well as closed two-phonon elastic processes [11]. Here, the first two result in transitions between the orbital levels and thus depolarization (γ_{\pm}), while the latter results in an AC-Stark type effect that can contribute to dephasing (γ_d).

The relation between orbital transition rates $\gamma_+ = \gamma_- \exp\left[-\frac{h\Delta_{12}}{k_B T}\right]$ is governed by the Boltzmann distribution [11] where h and k_B are the Planck and Boltzmann constants respectively, and T represents the temperature. The large $\Delta_{12} = 830$ GHz ground state splitting of SnVs has therefore an inverse effect on these rates at cryogenic temperatures. While a lower temperature reduces the thermal occupation of phonons that have sufficient energy to excite between the levels (γ_+), thermal relaxation from upper to lower orbital ground state (γ_-) occurs on a much faster timescale.

Directly measuring ultrafast events on the order of picoseconds in the time domain is challenging both in terms of control (pulse generation and synchronization) and photon detection jitter. A route to circumvent this is therefore to resolve these in the frequency domain instead, where the corresponding scales are much more resolvable.

CPT at $T = 4$ K provides a means to access information about the coherence properties of the orbital states in the spectral domain. In particular, through investigating the effects of different excitation powers, and comparing with a theoretical model, one can extract details about processes occurring on timescales that cannot be resolved with standard single photon detectors.

Within the scope of this work, only the orbital states are considered. For clarity, unless otherwise stated, all reported timescales and rates refer to orbital processes and not the spin. However, since the phononic processes are spin-preserving, the measured values also have a direct correspondence to spin coherence times. Dephasing between the spin levels occurs when a closed cycle of (spin-preserving) orbital transitions is complete and it is therefore possible to provide an upper bound for the spin dephasing time $T_{2, \text{spin}}^*$ by the T_+ ,

III. EXPERIMENTAL DETAILS

The Sn implanted diamond sample studied in this work is equipped with nanopillars. In the following measurements, two emitters E1 and E2 in different nanopillars are investigated. Further details about the sample, nanostructure fabrication, and emitter characterization are provided in the supplementary sec. S1 A.

For the following measurements, excitation light resonant with the SnV transitions are independently generated from two sources: from a CW dye laser (D laser), and a home-built second harmonic generation

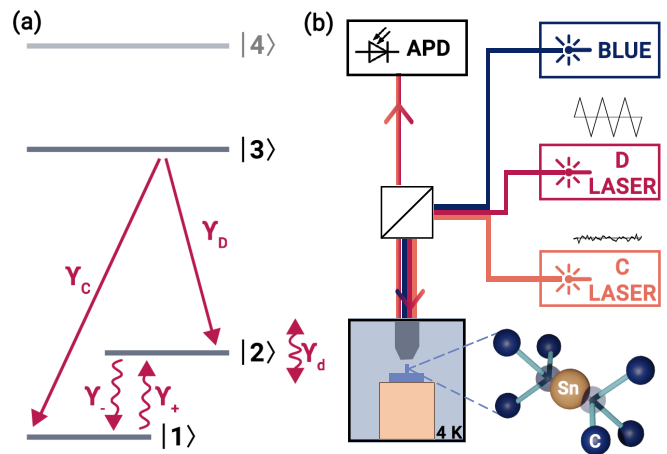


FIG. 1. (a) Orbital energy level structure and transitions of the SnV. γ_C and γ_D are the photonic relaxation (spontaneous emission) rates. γ_+ and γ_- are phononic excitation and relaxation (depolarization) processes, respectively. γ_d is the AC-Stark type dephasing process that is modelled as a decay of the second level onto itself. (b) Simplified schematic for the experimental setup. Blue laser is kept ON in the background to stabilize the charge environment and help with returning the resonance frequency to the set values after a hopping event occurs. C laser is tuned to the transition resonance and D laser scans the transition frequency in the coherent population trapping experiments. The emitter is located in a nanopillar that is cooled to 4 K. Collected fluorescence is measured with avalanche photodiodes (APD).

converted light from an infrared diode laser (C laser). They are combined with orthogonal linear polarization. This is desirable as C and D transition dipoles are expected to be orthogonal and would provide an efficient interaction [8]. Re-initialization light at 450 nm (blue) is provided by a commercial diode laser. These are combined into a fiber wavelength combiner and directed to the sample at $T = 4$ K through a scanning confocal setup. Emission from the sample is spectrally filtered and the phonon sideband is coupled into the detection fiber and directed to single-photon detectors. A simplified schematic of the experimental setup is presented in Fig. 1(b), and further details are provided in supplementary sec. S1 B.

IV. MEASUREMENTS

A. Temperature Dependent Linewidth Broadening

To gain insight into the interaction dynamics of an SnV with a phononic environment, linewidth measurements on the emitter E1 are conducted. At temperatures below 50 K, PLE spectra are measured with the blue laser continuously ON. The thermal/mechanical stability of the cryostat at elevated temperatures resulted in significant drift, and linewidths became broader than

the mode-hop free scan range of the laser. Therefore, the measurements at higher temperatures are recorded via photoluminescence (PL) spectra under non-resonant 520 nm green excitation.

For the PLE measurements, at every temperature, 10 to 20 frequency scans (in each scan direction) are conducted and histogrammed together. Since different scanning directions may have hysteresis effects, these are considered as distinct data sets. Furthermore, the investigated emitter was subject to spectral hops. A double Lorentzian function is used to capture the two observed resonance positions. The two lines are separately analyzed and their linewidths are averaged. Autocorrelation measurements confirm the single-emitter nature (see supplementary sec. S2 A).

The obtained linewidths are plotted in Fig. 2. The displayed cubic fit uses all the data points, while the linear fit only considers the data points up to 16 K. This cutoff is determined by checking the goodness-of-fit value by adding data points and monitoring a maxima value (see supplementary sec. S3). For the cubic fit, the linewidth at 0 K is constrained to match the value extracted from the linear fit (~ 200 MHz).

Previous studies have shown that for group-IV color centers, the dominant phonon interactions occur with E -symmetric modes, for which single-phonon processes broaden the linewidth with a linear temperature dependence, whereas the two-phonon elastic processes exhibit a cubic scaling with temperature [11]. Based on these evidence, we assume that, for the measurements and analyses at $T = 4$ K, the dephasing timescales are negligibly long compared to the orbital decays (within the linear regime of Fig. 2). However, since the ~ 400 MHz linewidth at 4 K is significantly broader than the lifetime-limited linewidth (~ 35 MHz [12]), a further test to validate this assumption is also included in the next section.

B. Orbital CPT

The CPT effect occurs when two transitions with a shared excited state are driven simultaneously in a lambda energy configuration (e.g. between levels 1, 2 and 3, coupled by transitions C and D, Fig. 1(a)). As one of the driving lasers is kept on resonance, a reduction in the fluorescence signal is observed when a second laser scans across the other transition frequency. Such a scheme results in bright and dark eigenstates, where only the bright state can be optically coupled to the excited state and produces a fluorescence signal. How much of the population becomes optically trapped in the dark state is determined by the coherence of these levels, and this directly influences the properties of the observed dip.

In these measurements, the C laser is kept resonant with the transition, while the D laser is scanned. Blue re-initialization light at 450 nm is applied throughout the scan. These measurements are performed twice

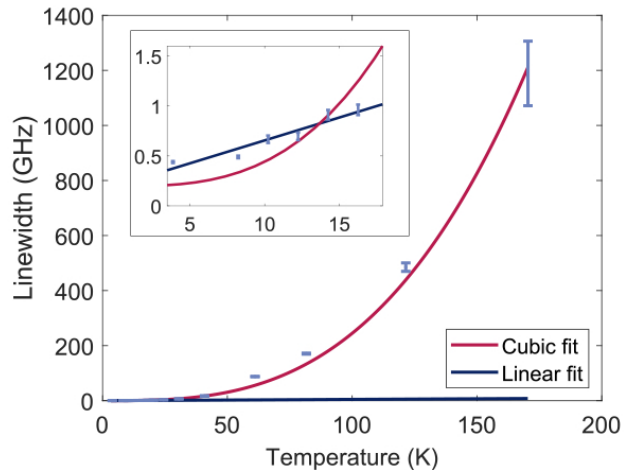


FIG. 2. Temperature dependence of the C transition linewidth (full width at half maximum). Measurements up to $T \leq 40$ K are obtained from PLE measurements scanning the laser across the transition. At higher temperatures, the widths are obtained from PL spectra as the widths exceed the scan range of the dye laser. The error bars are extracted from the Lorentzian fit uncertainties. INSET: At $T \lesssim 16$ K, the data points deviate from the cubic scaling observed at higher temperatures and the behaviour is well-described described by a linear fit. This suggests that two-phonon processes are suppressed in this regime.

(i.e. scanned in both directions) on emitter E2, using 9 different power configurations. The data are fit by numerically integrating a Lindblad master equation until the steady state is achieved (details of the model are provided in supplementary sec. S4 A). A direct correspondence between the powers and Rabi oscillations could not be used due to experimental instabilities (see supplementary sec. S1 B for details).

Therefore, these fits include three parameters: (i) Rabi frequency of the C transition Ω_C ; (ii) Rabi frequency of the D transition Ω_D ; and (iii) orbital phononic relaxation rate γ_- . A qualitative discussion of factors affecting the CPT profile is given in the supplementary sec. S4 B. There, it is shown that all three parameters have distinct effects on the CPT dip: Ω_C determines the offset of the CPT tail value, Ω_D affects both the linewidth and the contrast of the dip, and γ_- only affects the dip contrast. Distinct effects of the parameters enable a multidimensional fitting algorithm.

Here, γ_+ is related to γ_- by the thermalization rate determined by the Boltzmann distribution, and γ_d is set to 0. The latter constraint can be applied because at this temperature single phononic processes are expected to be dominant, as reflected in the linewidth measurements reported in the previous section.

Three example measurements and their fits are presented in Fig. 3. The steps of the data analysis and remaining measurements are presented in the supplementary sec. S4 C and S4 D respectively, and the

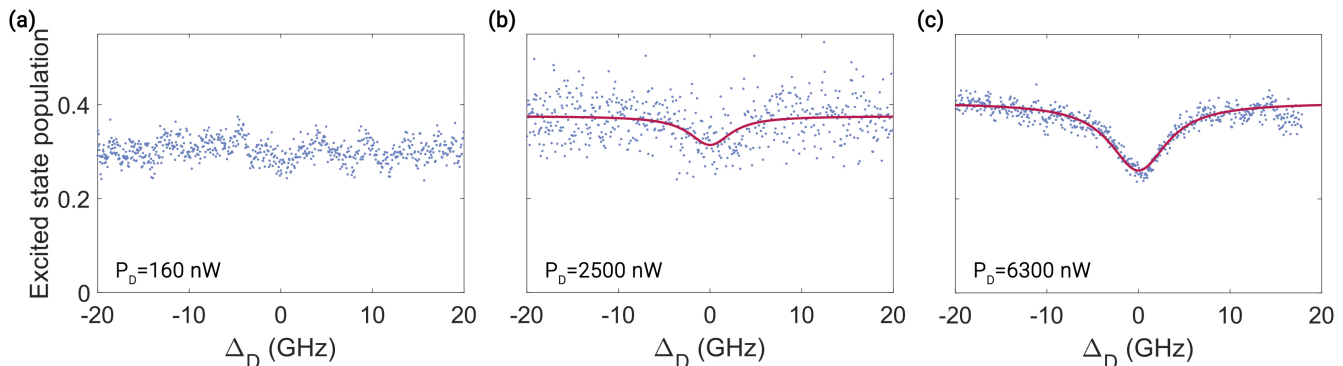


FIG. 3. Orbital CPT measurements at varying scanning laser power at D transition. The solid line is based on a fit from a Lindbladian master equation solution. Increasing the power results with a higher Rabi frequency on the D transition and allow the formation of a coherent dip against the rapid orbital decay process. Dataset indices from table I: (a) 13, (b) 9, (c) 17.

fit results are provided in appendix A at the end of the main text. The quoted powers are the powers incident at the cryostat window, measured at the beginning of each experiment. Out of 18 measurements, 16 measurements are taken into consideration for the estimation of γ_{\pm} , as in the limit of low excitation power (e.g. Fig. 3(a)) the signal is considered too small. On average (standard deviation), an orbital excitation time $T_{+} = 958$ (138) ns and orbital relaxation time $T_{-} = 31$ (5) ps are found, showing that the phononic relaxation is indeed an ultrafast process.

In order to estimate a bound for T_{2}^{*} , the orbital dephasing rate γ_{d} is increased (from 0) for each fit, until the dip visibility at zero detuning is reduced by 5%. Averaging (standard deviation) over the individual fits, 149 (84) ps is found to be the upper limit for which the dephasing process can still visibly affect the shape of the dip. This further demonstrates that CPT dip is mainly governed by the competition between γ_{-} and Ω_{D} and dephasing is not the dominant decoherence channel at this temperature for orbital qubits.

C. Phononic Relaxation Estimation from the D Transition Linewidth

Due to the fast thermal relaxation from the upper branch of the ground state, the population in level $|2\rangle$ is extremely low (less than 0.1%, using the extracted values from above). As such, locating, and resonantly exciting, the D transition can be challenging. For example, Fig. 4 shows a linewidth measurement for the D transition where a resonant power of ~ 1 μ W was required in order to detect any signal. This measurement resulted in a linewidth of $\Gamma_{D} = 5.406$ (43) GHz. These thermalized populations influence the CPT dips as well, and a minimum ~ 500 nW of power was needed to observe a dip.

As presented in section IV A for the C transition, the phononic coupling can broaden the linewidth of optical

transitions. While the C transition is protected from such effects at 4 K, the D transition is broadened by the rapid phononic relaxation. In [33], the authors theoretically quantify such linewidth broadening effects for G4Vs and estimate an SnV D transition linewidth of ~ 4000 GHz. Here, after accounting for spectral diffusion and power broadening (see supplementary sec. S5 for details) a phononic broadening component of $\Gamma_{D, \text{phon}} = 5.055$ (105) GHz is estimated from Fig. 4, which is within 25% of the predicted value. This value can also be converted to a relaxation timescale by $T_{-,D} = 1/(2\pi\Gamma_{D, \text{phon}}) = 31.7$ (7) ps. $T_{-,D}$ agrees very well with the T_{-} previously calculated from the orbital CPT measurements and thus confirms the timescale of the phononic processes.

V. CONCLUSION

Decoherence dynamics based on phononic interactions of SnV colors center are investigated in this letter. Linewidth broadening with temperature for SnV centers is measured to determine the single and two-phonon interaction regimes. We identify that single phonon processes are dominant at 4 K, and that a two-phonon cubic scaling starts dominating around 16 K. Through these measurements we also experimentally quantify, for the first time with an SnV, the phonon coupling rates at 4 K, the usual operating temperature for typical helium-cryostats. Consequently, the observed time scales are relevant for many applications.

CPT experiments are presented to show coherence between orbital levels and quantify the orbital phononic depolarization timescales. In particular, the orbital relaxation (γ_{-}), which occurs in a few tens of picoseconds, is indirectly measured in the frequency domain, as it is very demanding to probe such rapid events in the time domain. A time scale of 30 ps is ten times shorter than the electronic jitter of standard avalanche photodiodes. We therefore confirm

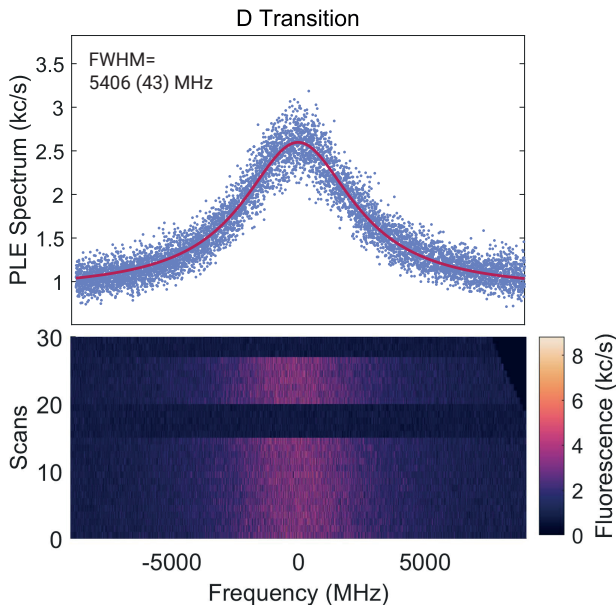


FIG. 4. PLE measurement at 4 K to identify the D transition linewidth of the emitter E2. Resonant laser power is set to 800 nW. A green laser with 1 μ W power is continuously on throughout the measurement for charge state stabilization. A Lorentzian function is used to fit the data for extracting the full width at half maximum (FWHM) and uncertainty. A spectral jump in the D transition is observed during the dark periods in the line scans. Since the population is very low in D due to thermalization, a high power is used to extract a signal. TOP: Histogrammed and fit count rates, BOTTOM: Frequency scans.

the improved resolution possible with CPT, an often-neglected advantage. We further verify the estimated rates by measuring the broadening induced by phononic processes to the D transition linewidth and extract a consistent result.

Our measurements directly indicate that the upper

branch of the SnV's orbital ground states is relatively short lived and therefore does not facilitate a practical qubit, similarly to previous observations with SiVs [34]. The increased ground state splitting limits the T_1 to the $T_1 \sim 30$ ps characterized in this work which is shorter than the coherence times of spin qubits.

The extracted T_+ value of 958 ns also yields insight into achievable $T_{2,\text{spin}}^*$ time scales as orbital excitation would provide an upper limit to the spin coherence times, when phonon-mediated dephasing is the limiting factor and other sources of dephasing (e.g. surrounding spin-bath [20] or gate-errors [18]) play a minor role. This relation shows that CPT at zero magnetic field is a valuable method to estimate spin qubit decoherence, without directly accessing the levels themselves.

ACKNOWLEDGMENTS

The authors would like to thank Mariano Isaza Monsalve for insightful discussions regarding CPT dynamics; Laura Orphal-Kobin for sharing her experience as the PLE scans were implemented; Kilian Unterguggenberger with discussions regarding linewidth data analyses; Maarten van der Hoeven for his help setting the laser infrastructure; Mathias Matalla, Natalia Kemf, Nico Sluka and Karina Ickert for support with lithography; Ina Ostermay, Adrian Runge and Dominik Sudau for performing the SiNx deposition; Alex Kühlberg for performing the ion implantation; Ralph-Stephan Unger, Kevin Kunkel and Natalia Sabelfeld for their support with the plasma etching.

The authors acknowledge funding by the European Research Council (ERC, Starting Grant project QUREP, No. 851810), the German Federal Ministry of Education and Research (BMBF, project DiNOQuant, No. 13N14921; project QPIS, No. 16KISQ032K; project QPIC-1, No. 13N15858), and the Einstein Foundation Berlin (Einstein Research Unit on Quantum Devices).

-
- [1] K. Senkalla, G. Genov, M. H. Metsch, P. Siyushev, and F. Jelezko, Germanium Vacancy in Diamond Quantum Memory Exceeding 20 ms, [arXiv preprint , 2308.09666 \(2023\)](#).
 - [2] C. M. Knaut, A. Suleymanzade, Y.-C. Wei, D. R. Assumpcao, P.-J. Stas, Y. Q. Huan, B. Machielse, E. N. Knall, M. Sutula, G. Baranes, N. Sinclair, C. De-Eknamkul, D. S. Levonian, M. K. Bhaskar, H. Park, M. Lončar, and M. D. Lukin, Entanglement of Nanophotonic Quantum Memory Nodes in a Telecommunication Network, [arXiv preprint , 2310.01316 \(2023\)](#).
 - [3] U. Wahl, J. G. Correia, R. Villarreal, E. Bourgeois, M. Gulka, M. Nešládek, A. Vantomme, and L. M. C. Pereira, Direct Structural Identification and Quantification of the Split-Vacancy Configuration for Implanted Sn in Diamond, [Physical Review Letters **125**, 045301 \(2020\)](#).
 - [4] L. Orphal-Kobin, K. Unterguggenberger, T. Pregolato, N. Kemf, M. Matalla, R.-S. Unger, I. Ostermay, G. Pieplow, and T. Schröder, Optically Coherent Nitrogen-Vacancy Defect Centers in Diamond Nanostructures, [Physical Review X **13**, 011042 \(2023\)](#).
 - [5] A. Sipahigil, K. D. Jahnke, L. J. Rogers, T. Teraji, J. Isoya, A. S. Zibrov, F. Jelezko, and M. D. Lukin, Indistinguishable photons from separated silicon-vacancy centers in diamond, [Physical Review Letters **113**, 113602 \(2014\)](#).
 - [6] Y. Narita, P. Wang, K. Ikeda, K. Oba, Y. Miyamoto, T. Taniguchi, S. Onoda, M. Hatano, and T. Iwasaki, Multiple Tin-Vacancy Centers in Diamond with Nearly Identical Photon Frequency and Linewidth, [Physical Review Applied **19**, 024061 \(2023\)](#).
 - [7] J. M. Bopp, M. Plock, T. Turan, G. Pieplow, S. Burger,

- and T. Schröder, 'Sawfish' Photonic Crystal Cavity for Near-Unity Emitter-to-Fiber Interfacing in Quantum Network Applications, [arXiv preprint](#) , [2201.02731 \(2022\)](#).
- [8] A. E. Rugar, C. Dory, S. Sun, and J. Vučković, Characterization of optical and spin properties of single tin-vacancy centers in diamond nanopillars, [Physical Review B](#) **99**, 205417 (2019).
- [9] J. Arjona Martínez, R. A. Parker, K. C. Chen, C. M. Purser, L. Li, C. P. Michaels, A. M. Stramma, R. Debroux, I. B. Harris, M. Hayhurst Appel, E. C. Nichols, M. E. Trusheim, D. A. Gangloff, D. Englund, and M. Atatüre, Photonic Indistinguishability of the Tin-Vacancy Center in Nanostructured Diamond, [Physical Review Letters](#) **129**, 173603 (2022).
- [10] C. T. Nguyen, D. D. Sukachev, M. K. Bhaskar, B. Machielse, D. S. Levonian, E. N. Knall, P. Stroganov, C. Chia, M. J. Burek, R. Riedinger, H. Park, M. Lončar, and M. D. Lukin, An integrated nanophotonic quantum register based on silicon-vacancy spins in diamond, [Phys. Rev. B](#) **100**, 165428 (2019).
- [11] K. D. Jahnke, A. Sipahigil, J. M. Binder, M. W. Doherty, M. Metsch, L. J. Rogers, N. B. Manson, M. D. Lukin, and F. Jelezko, Electron-phonon processes of the silicon-vacancy centre in diamond, [New Journal of Physics](#) **17**, 043011 (2015), [arXiv:1411.2871](#).
- [12] M. E. Trusheim, B. Pingault, N. H. Wan, M. Gündoğan, L. de Santis, R. Debroux, D. Gangloff, C. Purser, K. C. Chen, M. Walsh, J. J. Rose, J. N. Becker, B. Lienhard, E. Bersin, I. Paradeisanos, G. Wang, D. Lyzwa, A. R.-P. Montblanch, G. Malladi, H. Bakhru, A. C. Ferrari, I. A. Walmsley, M. Atatüre, and D. Englund, Transform-Limited Photons From a Coherent Tin-Vacancy Spin in Diamond, [Physical Review Letters](#) **124**, 023602 (2020).
- [13] M. H. Abobeih, J. Cramer, M. A. Bakker, N. Kalb, M. Markham, D. J. Twitchen, and T. H. Taminiau, One-second coherence for a single electron spin coupled to a multi-qubit nuclear-spin environment, [Nature Communications](#) **9**, 2552 (2018).
- [14] X. Guo, A. M. Stramma, Z. Li, W. G. Roth, B. Huang, Y. Jin, R. A. Parker, J. A. Martínez, N. Shofer, C. P. Michaels, C. P. Purser, M. H. Appel, E. M. Alexeev, T. Liu, A. C. Ferrari, D. D. Awschalom, N. Deegan, B. Pingault, G. Galli, F. J. Heremans, M. Atatüre, and A. A. High, Microwave-based quantum control and coherence protection of tin-vacancy spin qubits in a strain-tuned diamond membrane heterostructure, [arXiv preprint](#) , [2307.11916 \(2023\)](#).
- [15] B. Pingault, D.-D. Jarausch, C. Hepp, L. Klintberg, J. N. Becker, M. Markham, C. Becher, and M. Atatüre, Coherent control of the silicon-vacancy spin in diamond, [Nature Communications](#) **8**, 15579 (2017).
- [16] P. Siyushev, M. H. Metsch, A. Ijaz, J. M. Binder, M. K. Bhaskar, D. D. Sukachev, A. Sipahigil, R. E. Evans, C. T. Nguyen, M. D. Lukin, P. R. Hemmer, Y. N. Palyanov, I. N. Kupriyanov, Y. M. Borzdov, L. J. Rogers, and F. Jelezko, Optical and microwave control of germanium-vacancy center spins in diamond, [Physical Review B](#) **96**, 081201 (2017).
- [17] E. I. Rosenthal, C. P. Anderson, H. C. Kleidermacher, A. J. Stein, H. Lee, J. Grzesik, G. Scuri, A. E. Rugar, D. Riedel, S. Aghaeimeibodi, G. H. Ahn, K. Van Gasse, and J. Vučković, Microwave Spin Control of a Tin-Vacancy Qubit in Diamond, [Physical Review X](#) **13**, 031022 (2023).
- [18] R. Debroux, C. P. Michaels, C. M. Purser, N. Wan, M. E. Trusheim, J. Arjona Martínez, R. A. Parker, A. M. Stramma, K. C. Chen, L. de Santis, E. M. Alexeev, A. C. Ferrari, D. Englund, D. A. Gangloff, and M. Atatüre, Quantum Control of the Tin-Vacancy Spin Qubit in Diamond, [Physical Review X](#) **11**, 041041 (2021).
- [19] D. D. Sukachev, A. Sipahigil, C. T. Nguyen, M. K. Bhaskar, R. E. Evans, F. Jelezko, and M. D. Lukin, Silicon-Vacancy Spin Qubit in Diamond: A Quantum Memory Exceeding 10 ms with Single-Shot State Readout, [Physical Review Letters](#) **119**, 223602 (2017).
- [20] J. N. Becker, B. Pingault, D. Groß, M. Gündoğan, N. Kukharchyk, M. Markham, A. Edmonds, M. Atatüre, P. Bushev, and C. Becher, All-Optical Control of the Silicon-Vacancy Spin in Diamond at Millikelvin Temperatures, [Physical Review Letters](#) **120**, 053603 (2018).
- [21] J. Görlitz, D. Herrmann, G. Thiering, P. Fuchs, M. Gandil, T. Iwasaki, T. Taniguchi, M. Kieschnick, J. Meijer, M. Hatano, A. Gali, and C. Becher, Spectroscopic investigations of negatively charged tin-vacancy centres in diamond, [New Journal of Physics](#) **22**, 013048 (2020).
- [22] E. Neu, D. Steinmetz, J. Riedrich-Möller, S. Gsell, M. Fischer, M. Schreck, and C. Becher, Single photon emission from silicon-vacancy colour centres in chemical vapour deposition nano-diamonds on iridium, [New Journal of Physics](#) **13**, 025012 (2011).
- [23] T. Iwasaki, Y. Miyamoto, T. Taniguchi, P. Siyushev, M. H. Metsch, F. Jelezko, and M. Hatano, Tin-Vacancy Quantum Emitters in Diamond, [Phys. Rev. Lett.](#) **119**, 253601 (2017).
- [24] R. A. Parker, J. A. Martínez, K. C. Chen, A. M. Stramma, I. B. Harris, C. P. Michaels, M. E. Trusheim, M. H. Appel, C. M. Purser, W. G. Roth, D. Englund, and M. Atatüre, A diamond nanophotonic interface with an optically accessible deterministic electronuclear spin register, [arXiv preprint](#) , [2305.18923 \(2023\)](#).
- [25] G. Clark, H. Raniwala, M. Koppa, K. Chen, A. Leenheer, M. Zimmermann, M. Dong, L. Li, Y. H. Wen, D. Dominguez, M. Trusheim, G. Gilbert, M. Eichenfield, and D. Englund, Nanoelectromechanical control of spin-photon interfaces in a hybrid quantum system on chip, [arXiv preprint](#) , [2308.07161 \(2023\)](#).
- [26] C. Santori, P. Tamarat, P. Neumann, J. Wrachtrup, D. Fattal, R. G. Beausoleil, J. Rabeau, P. Olivero, A. D. Greentree, S. Praver, F. Jelezko, and P. Hemmer, Coherent population trapping of single spins in diamond under optical excitation, [Physical Review Letters](#) **97**, 247401 (2006).
- [27] B. Pingault, J. N. Becker, C. H. H. Schulte, C. Arend, C. Hepp, T. Godde, A. I. Tartakovskii, M. Markham, C. Becher, and M. Atatüre, All-optical formation of coherent dark states of silicon-vacancy spins in diamond, [Physical Review Letters](#) **113**, 263601 (2014).
- [28] L. J. Rogers, K. D. Jahnke, M. H. Metsch, A. Sipahigil, J. M. Binder, T. Teraji, H. Sumiya, J. Isoya, M. D. Lukin, P. Hemmer, and F. Jelezko, All-optical initialization, readout, and coherent preparation of single silicon-vacancy spins in diamond, [Physical Review Letters](#) **113**, 263602 (2014).
- [29] J. Görlitz, D. Herrmann, P. Fuchs, T. Iwasaki, T. Taniguchi, D. Rogalla, D. Hardeman, P.-O. Colard,

- M. Markham, M. Hatano, and C. Becher, Coherence of a charge stabilised tin-vacancy spin in diamond, *npj Quantum Information* **8**, 1 (2022).
- [30] T. M. Babinec, B. J. M. Hausmann, M. Khan, Y. Zhang, J. R. Maze, P. R. Hemmer, and M. Loncar, A diamond nanowire single-photon source, *Nature Nanotechnology* **5**, 195 (2010).
- [31] A. E. Rugar, C. Dory, S. Sun, and J. Vučković, Characterization of optical and spin properties of single tin-vacancy centers in diamond nanopillars, *Physical Review B* **99**, 205417 (2019).
- [32] G. m. H. Thiering and A. Gali, Ab Initio Magneto-Optical Spectrum of Group-IV Vacancy Color Centers in Diamond, *Phys. Rev. X* **8**, 021063 (2018).
- [33] P. Wang, L. Kazak, K. Senkalla, P. Siyushev, R. Abe, T. Taniguchi, S. Onoda, H. Kato, T. Makino, M. Hatano, F. Jelezko, and T. Iwasaki, Transform-Limited Photon Emission From a Lead-Vacancy Center in Diamond Above 10 K, *arXiv preprint*, 2308.00995 (2023).
- [34] J. N. Becker, J. Görlitz, C. Arend, M. Markham, and C. Becher, Ultrafast all-optical coherent control of single silicon vacancy colour centres in diamond, *Nature Communications* **7**, 13512 (2016).

Appendix A: Fit Results

Dataset Index	Laser power (nW)			Extracted fit parameters:			
	C	D	BLUE	Ω_C (2π MHz)	Ω_D (2π MHz)	T_+ (ns)	T_- (ps)
1	4	1300	2500	7.1 (3)	110 (14)	954 (559)	31 (18)
2	4	1300	2500	7.1 (3)	115 (15)	915 (547)	30 (18)
3	4	1500	2500	5.3 (2)	104 (11)	1156 (726)	38 (24)
4	4	1500	2500	5.3 (2)	112 (14)	846 (499)	27 (16)
5	10	1800	2500	9.4 (4)	124 (17)	855 (489)	28 (16)
6	10	1800	2500	9.4 (4)	99 (14)	1326 (762)	43 (25)
7	18	1800	2500	13.0 (6)	159 (15)	987 (651)	32 (21)
8	18	1800	2500	12.8 (6)	177 (13)	1036 (727)	34 (24)
9	30	2500	2500	19.3 (14)	164 (24)	966 (552)	31 (18)
10	30	2500	2500	20.4 (17)	164 (26)	921 (493)	30 (16)
11	95	6000	4000	20.1 (10)	272 (13)	994 (741)	32 (24)
12	95	6000	4000	19.3 (9)	296 (14)	869 (652)	28 (21))
13	100	160	5800	–	–	–	–
14	100	160	5800	–	–	–	–
15	110	1500	2500	82 (20)	417 (65)	862 (477)	28 (15)
16	110	1500	2500	74 (18)	353 (58)	1048 (569)	34 (18)
17	100	6300	2500	22.9 (13)	306 (16)	807 (595)	26 (19)
18	100	6300	2500	22.4 (13)	307 (16)	785 (579)	25 (19)
Average (Standard dev.)						958 (138)	31 (5)

TABLE I. Tabulated summary of the coherent population trapping experiments. Subsequent measurements with the same laser parameters are two different scan directions (odd (even): low to high (high to low) frequencies). The quoted laser powers are measured at the beginning of the experiments and subjected to drifts during the scans. Combined with instability of the sample position, varying Rabi frequencies (Ω) to power relations are observed. Provided uncertainties are the 5% parameter sensitivities at the two-photon resonance (see supplementary sec. S4C). Resulting orbital level lifetimes (T_{\pm}) are averaged in the end.

Supplementary to optical probing of phononic properties of a tin-vacancy color center in diamond

Cem Güney Torun,^{1,*} Joseph H. D. Munns,^{1,*} Franziska Marie Herrmann,¹ Viviana Villafane,^{2,3}
Kai Müller,³ Andreas Thies,⁴ Tommaso Pregnolato,^{1,4} Gregor Pieplow,¹ and Tim Schröder^{1,4,†}

¹*Department of Physics, Humboldt-Universität zu Berlin, 12489 Berlin, Germany*

²*Walter Schottky Institute, School of Natural Sciences and MCQST,
Technische Universität München, 85748 Garching, Germany*

³*Walter Schottky Institute, School of Computation, Information and Technology and MCQST,
Technische Universität München, 85748 Garching, Germany*

⁴*Ferdinand-Braun-Institut gGmbH, Leibniz-Institut für Höchstfrequenztechnik, 12489 Berlin, Germany*

S1. EXPERIMENTAL DETAILS

A. Sample

The sample used in this work is an electronic grade, single-crystal diamond grown by chemical vapor deposition (supplied by Element Six Technologies Ltd. (UK) and with $\{100\}$ faces). The substrate is initially cleaned for about one hour in a boiling triacid solution ($\text{H}_2\text{SO}_4:\text{HNO}_3:\text{HClO}_4$, 1:1:1) [1] and then etched in Cl_2/He and O_2/CF_4 plasmas, in order to remove any organic contaminants and structural defects from the surface [2]. Tin ions are subsequently implanted in the diamond, by employing the following nominal parameters: fluence of 5×10^{10} atoms cm^{-2} and implantation energy of 400 keV. Stopping and Range of Ions in Matter [3] simulations estimate a penetration depth of about 100 nm with this energy. Finally, an annealing step performed at a temperature $T = 1050$ °C for about 12 hours and at a pressure $P < 7.5 \times 10^{-8}$ mbar activates the diffusions of the vacancies in the diamond lattice and the formation of the negatively-charged tin vacancy (SnV^-) color centers.

Nanopillars are fabricated by a combination of e-beam lithography and plasma etching. First, 200 nm of SiN_x are deposited on the surface of the diamond in an inductively coupled-plasma enhanced chemical vapor deposition system. After spin-coating the sample with 300 nm of electro-sensitive resist (ZEP520A), we expose pillars with nominal diameters ranging from 180 nm to 340 nm, in steps of 40 nm. After development, the pattern is transferred into the SiN_x layer by a reactive ion etching (RIE) plasma (10 sccm CF_4 , RF power = 100 W, P = 1 Pa) and then etched into the diamond during an ICP process in O_2 plasma (80 sccm, ICP power = 750 W, RF power = 200 W, P = 0.3 Pa). The remaining nitride layer is finally removed in a solution of buffered HF.

B. Optical Setup

The employed experimental setup is illustrated in Fig. S1. Resonant excitation lights (at 619 nm) are generated from a continuous wave dye laser (Sirah Matisse, DCM in EPL/EG solution) and home-built second harmonic generation (SHG) source converted from a 1238 nm diode (Innolume dfb-1238-pm-40-OI, Covesion MSHG-1230-0.5-4). The SHG source provides a simple and cost-effective alternative to dye or optical parametric oscillator based sources at 619 nm, in a wavelength region where no commercial diode lasers exist. These beams are overlapped orthogonally in polarization on a beamsplitter and fiber coupled. In the overlap setup, the power of the resonant lasers can be controlled with the half-wave plates. The leak-through is then monitored on a wavemeter (High Finesse WS7). In addition to the resonant lasers, a re-initialization blue laser at 450 nm (Thorlabs LP450-SF15) and non-resonant excitation green laser at 520 nm (DLnSec) are combined into the same mode as the resonant excitation in a fiber wavelength combiner. Experiments are controlled via the Qudi [4] software suite.

The excitation mode is directed to the sample in a closed-cycle helium cryostat (Montana s50) at 4 K via a home-built confocal scanning microscopy setup with an objective (Zeiss) of 0.9 numerical aperture. A quarter- and half-wave plate combination is employed to optimize the laser polarizations with respect to the SnV transition polarizations, where the C and D dipoles are orthogonal for a (100) terminated sample.

* These authors contributed equally to this work

† Corresponding author: tim.schroeder@physik.hu-berlin.de

For the coherent population trapping (CPT) and photoluminescence excitation (PLE) measurements a long-pass filter at 635 nm is used to filter the laser light, and the phonon sideband is coupled to the detection fiber. In photoluminescence (PL) measurements, a long-pass filter at 600 nm is used instead. In the detection fiber, the signal is split through a 50:50 fiber beam-splitter, where one port is used to monitor the signal counts (Excelitas SPCM-AQ4C), and the other port is either directed to a second channel on the APD for autocorrelation measurements, or to a spectrometer (Princeton Instruments Teledyne SpectraPro HRS500) for PL spectrum measurements.

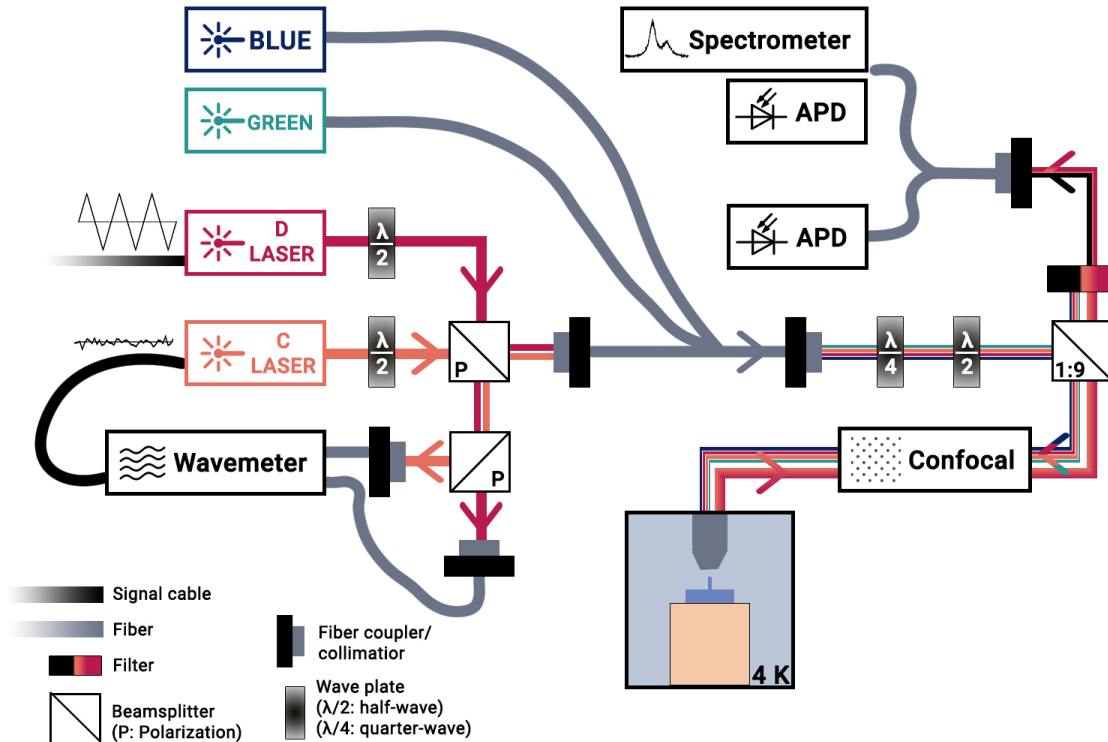


FIG. S1. Schematic of the experimental setup. Four different lasers are used in this work. Resonant lasers are overlapped orthogonally on a polarization beamsplitter and fiber coupled. The beams from the other port of the overlap beamsplitter are then once split on a second polarization beamsplitter and monitored via a wavemeter to determine their frequencies. Three fibers with four laser beams are combined spatially on a fiber combiner. Through a 4f confocal microscopy setup, the sample with nanopillars is scanned at 4 K temperature. Collected fluorescence is spectrally filtered from the excitation lasers, and directed to avalanche photo diodes (APDs) or spectrometers.

System instabilities: On different CPT measurements SHG system (C laser) has shown inconsistent changes of power from 10% to 50% from the beginning to end of the measurements ranging on measurements that took around 3 hours. In a separate characterization measurement the dye laser (D laser) showed typical power drifts up to $\pm 40\%$ in 30 minutes. Furthermore, during the scans dye laser is expected to have a varying power as the lasing efficiency is frequency dependent.

While no power stability schemes are implemented on either laser, SHG (C laser) frequency is stabilized using a PID loop and showed 6.4 MHz standard deviation over the course of a ~ 6 hour-long measurement.

During the measurements, inconsistent drifts on the x-y position of the sample up to ~ 100 nm/hour is observed. One of the reason for these drifts is likely the scanning (galvo) mirrors not being in a temperature stabilized environment (attocube sample stages in the cryostat are expected to have a higher long-term stability). Drops in the fluorescence signal of $\sim 10\%$ /hour is also observed due to the fiber coupling mirrors remaining in a not temperature-stabilized environment.

Finally, while not quantified, z-focus of the sample that is controlled with the z-axis attocube stage is observed to drift over time and required optimization similarly with the x-y position. This error is attributed to the heaters not perfectly stabilizing the objective lens in the cryostat to the room temperature (over 100 mK oscillations have been observed). It is expected that this problem further contributed to the irregular shifts in the x-y plane as well. After the experiments were completed, the heater issue was fixed and consequently the z-axis focus problem was resolved and further stability on the x-y positioning was observed.

S2. EMITTER CHARACTERISATION

In this work, the results from two different nanopillars are presented. Investigations regarding the temperature-dependent linewidths (main text sec. IV A) are done with the emitter E1. The CPT and D transition linewidth broadening experiments (main text sec. IV B and IV C) are done on emitter E2. However, E2 stopped fluorescing after these measurements were completed.

A. Emission autocorrelation

In order to confirm the investigated emitters are indeed single, an autocorrelation measurement using a Hanbury Brown-Twiss interferometer configuration is carried out. Collected fluorescence under non-resonant excitation is split via a fiber beamsplitter and the coincidences from two ports are correlated. Then the autocorrelation data are fit using the following equation [5]:

$$g^{(2)}(\tau) = 1 + p^2 \left[c \exp\left(\frac{-|\tau - o|}{\tau_b}\right) - (1 + c) \exp\left(\frac{|\tau - o|}{\tau_a}\right) \right], \quad (1)$$

where p , c , τ_a (antibunching time), τ_b (bunching time) and o (detector offset) are fitting parameters; and τ is the delay.

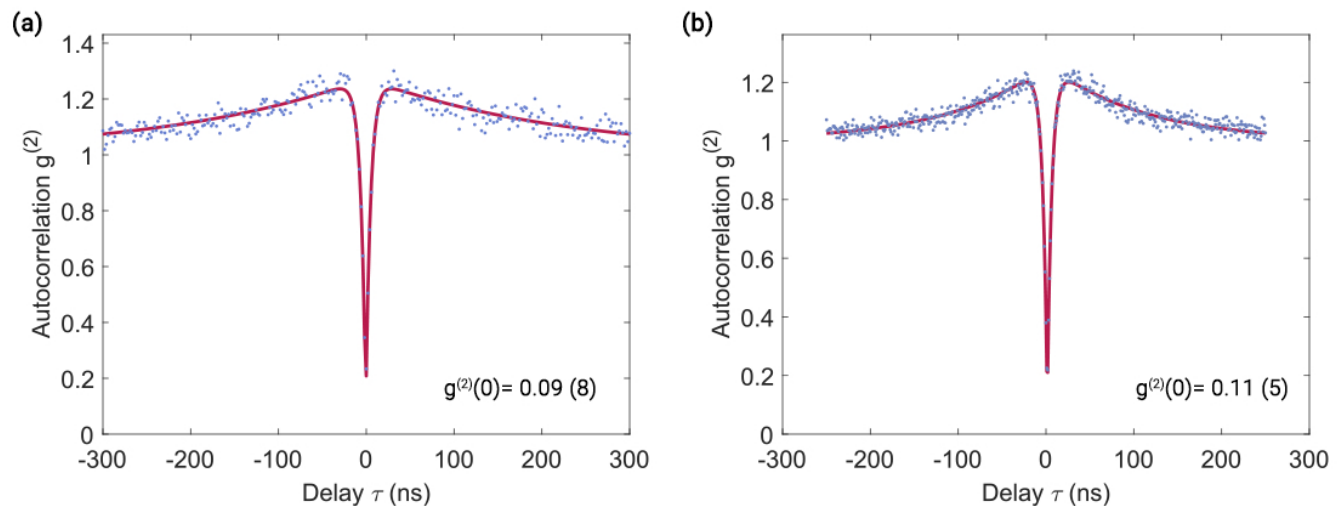


FIG. S2. Autocorrelation measurements under 520 nm, 500 μ W non-resonant excitation for emitters (a) E1 (b) E2. The extracted $g^{(2)}(0)$ values confirm that the investigated nanopillars contain single emitters coupling to their nanostructures.

B. Spectroscopy

Here, PL and PLE spectra of both emitters are provided as characterization measurements of the emitters. PLE linewidth indicates the quality of the emitter, as a smaller value would mean higher indistinguishability of the emitted photons, a weaker coupling to the charge environment, and less strain around the emitters. PL spectrum is utilized to extract information about the branching from the excited state decay for the emitter E2.

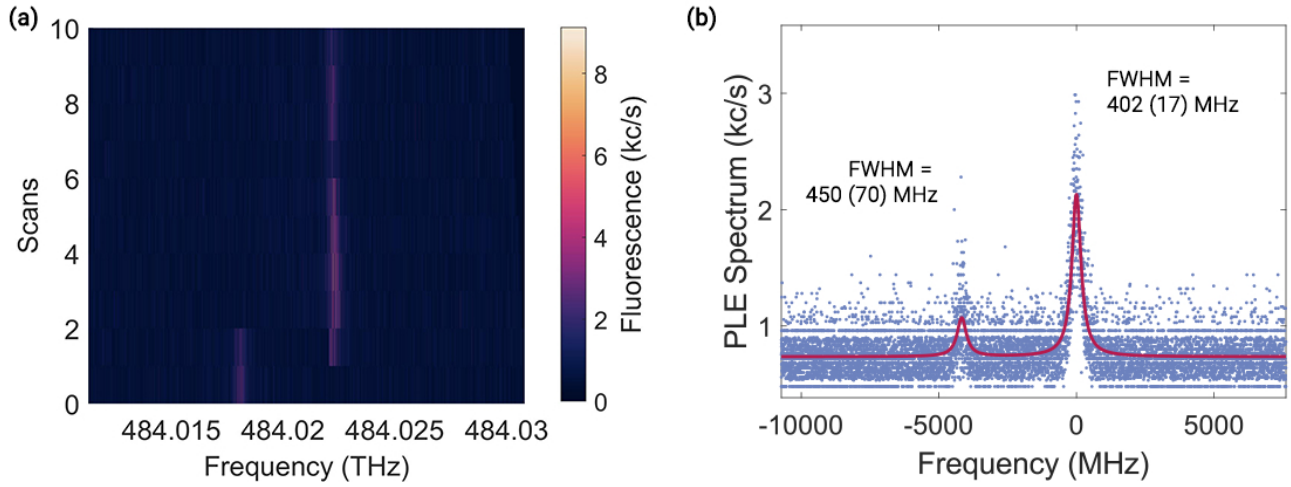


FIG. S3. PLE measurement at 4 K to identify the C transition linewidth of the emitter E1. Resonant and blue laser powers are set to 0.5 nW, and 1 μ W respectively. Blue laser is ON throughout the measurement. A spectral jump at the second line scan is observable. (a) Frequency line scans (b) Histogrammed and fit count rates using a double Lorentzian function. Uncertainties are extracted from the fit.

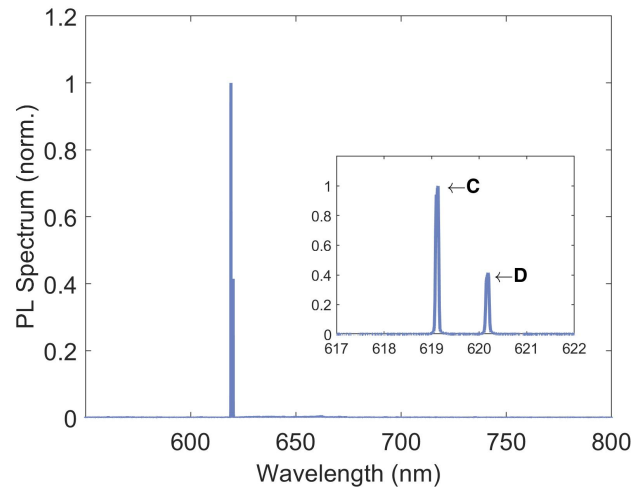


FIG. S4. PL spectrum measurement of the emitter E2 at 4 K under 520 nm green non-resonant excitation. The peak height ratio of 2.4 (1) is extracted for estimating individual spontaneous emission rates in both transitions.

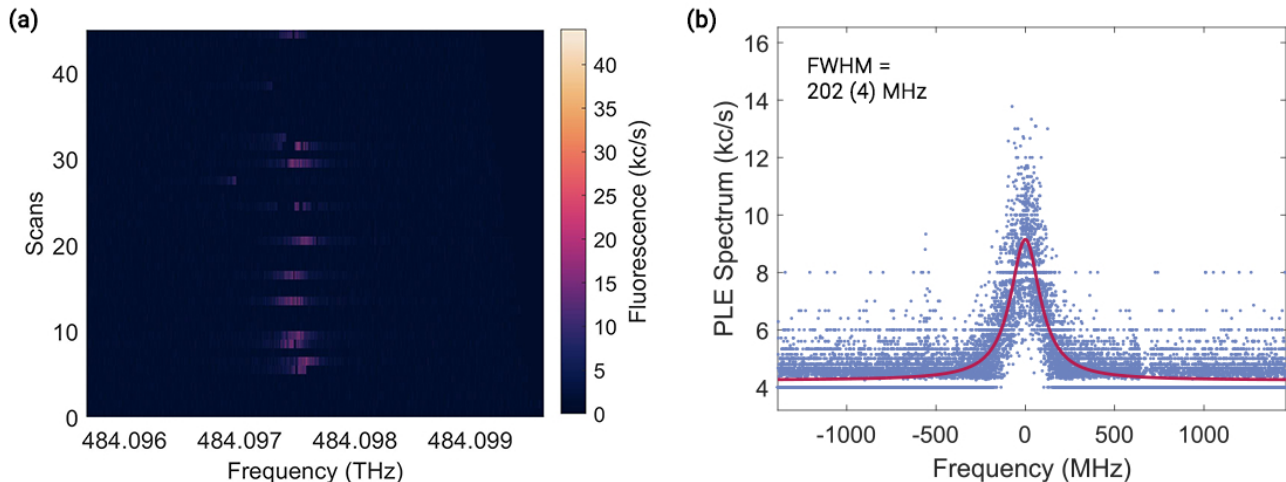


FIG. S5. PLE measurement at 4 K to identify the C transition linewidth of the emitter E2. Resonant (C) and blue laser powers are set to 0.5 nW, and 375 nW respectively. Blue laser is pulsed at the beginning of every scan for 10 ms. (a) Frequency scans. (b) Histogrammed and fit count rates using a Lorentzian function. The uncertainty is extracted from the fit.

C. Lifetime

One of the parameters that are required in CPT modelling is the lifetime τ_{se} of the excited state. A resonant pulsed excitation shorter than the lifetime (~ 150 fs) is implemented. The fluorescence response is fit to an exponential $\exp(-\frac{1}{\tau_{se}}t)$ to extract the time t it takes on average for the emitter to spontaneously emit.

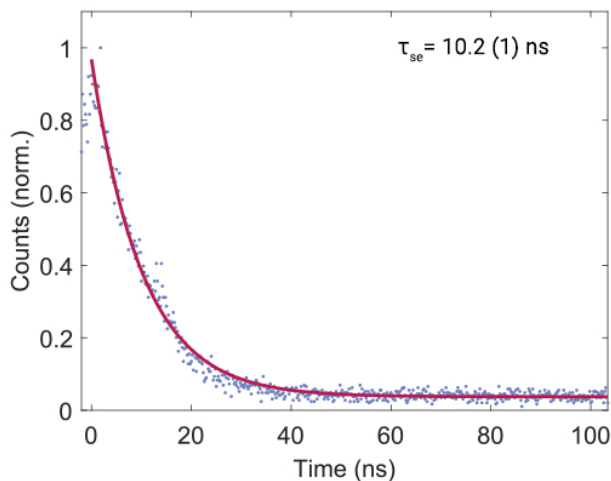


FIG. S6. Histogrammed fluorescence signal measurements after repetitive resonant 150 fs pulsed excitations. Before the excitation, a 500 ns green laser pulse is sent to initialize the charge state of the SnV. An exponential decay fit reveals the photonic lifetime of level $|3\rangle$. This value is used to estimate the combined spontaneous emission rate of the C and D transitions and employed in the CPT model.

D. Saturation

Translating fluorescence signals to the excited state populations requires an estimation of the saturation intensity. With this purpose, the fluorescence signal at the beginning of each CPT measurement is extracted using the average of the first 100 data points (where the D transition detuning is very large and fluorescence from D transition is negligible) are extracted, and the error bars are estimated from the standard deviation of these data. This method

had to be implemented as the emitter stopped fluorescing before a usual power versus count rate measurement could be performed.

By pairing the extracted fluorescence counts with the C laser powers at the beginning of each measurement, the saturation fluorescence is estimated using the following equation:

$$F(P) = \frac{F_{\text{sat}}P}{P_{\text{sat}} + P} + 0.5, \quad (2)$$

where F_{sat} (saturation intensity) and P_{sat} (saturation power) are the fitting parameters; P is the power; and 0.5 is selected as the background correction due the dark counts (from APD specifications).

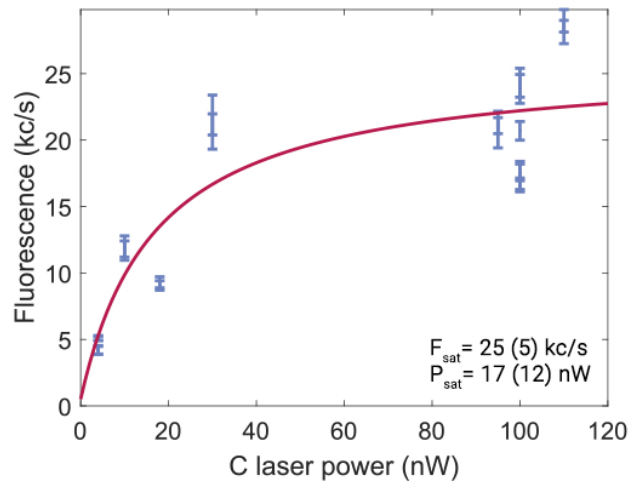


FIG. S7. Saturation curve for the emitter E2, using the data extracted from the CPT experiments. Error bars are the standard deviation of 100 data points employed to estimate the average countrate.

S3. R-SQUARED ANALYSIS

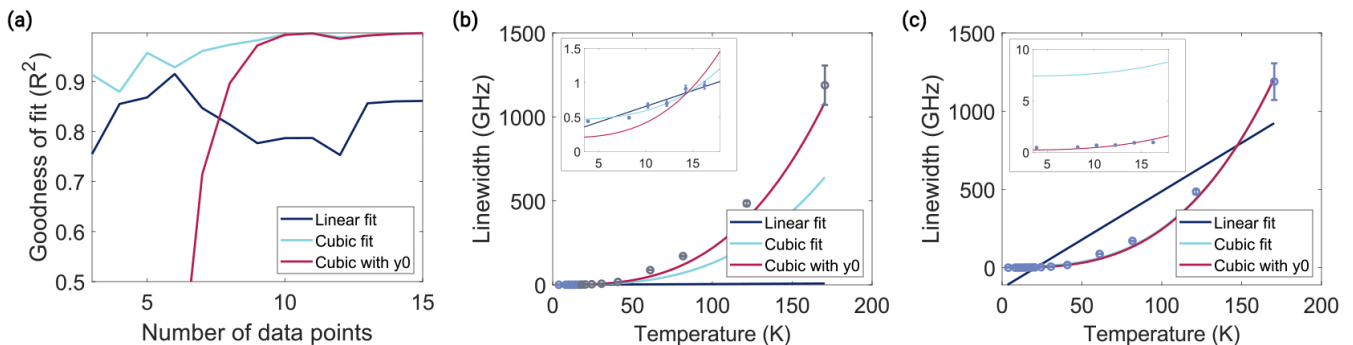


FIG. S8. (a) Goodness of fit value with increasing data points for three different fitting strategies to model the linewidth broadening with increasing temperature. Functions: Linear fit $ax+b$, Cubic fit: ax^3+b , Cubic fit with y_0 : ax^3+y_0 , where a and b are fitting parameters, and y_0 is pre-selected as b extracted from the linear fit. A local maxima for linear fit is observable at the 6th (16 K) data point. (b) Three different fits generated by only taking the first six data points into consideration (gray points are excluded). Neither of the fits can describe the whole temperature range well by themselves. (c) Three different fits generated by taking all the data points into consideration. Once again, neither of the fits can describe the whole temperature range well, suggesting two different fits are required to describe the process.

In the main text, the linewidth broadening with increasing temperature is investigated to identify the regimes where the broadening is linear and where it is cubic. These trends give clues about the phononic processes as in the linear regime single phonon events (depolarization) is dominant, and the cubic regime is governed by two-phonon

(dephasing) events. With this purpose, the data are analyzed to justify the hypothesis that a single linear or cubic polynomial (without quadratic and linear terms) can not represent the broadening mechanisms by themselves. Also here, it has been attempted to identify a cutoff temperature where the linear trend starts to be cubic.

With these motivations, three different fitting strategies have been identified to model the linewidth broadening with temperature: i) 'Linear fit': $ax + b$, where a and b are fitting parameters, ii) 'Cubic fit': $ax^3 + b$, where a and b are fitting parameters, iii) 'Cubic with y_0 ': $ax^3 + y_0$, where a is the fitting parameter, and y_0 is pre-selected from the b parameter that is extracted from the linear fit. In Fig. S8(a), the goodness of fit value (R^2) is extracted for each fitting strategy as the next data points are included in the fitting parameter. A local maximum at the sixth data point (16 K) for the linear fit is identified from the figure, and picked as the cut-off.

Next, the fitting strategies are tested via i) using extracted fits from the first 6 data points as shown in Fig. S8(b), ii) using extracted fits from all data points as shown in Fig. S8(c). Inset of Fig. S8(b) shows both linear and cubic fits can successfully represent the data, with the cubic function performing slightly better with the R^2 value (see Fig. S8(a)). However, a cubic fit from only the first 6 data points can not predict the next 9 values very well and diverges from measurements. Interestingly, when a cubic fit is used to model the whole data set, it diverges significantly from the first six data points shown in the inset of S8(c). The reason for this is the fitting algorithm trying to normal distribute the errors as well as minimize them. Compensating higher errors from higher temperatures results with an offset at the lower ones. This is where the third fitting strategy comes into play and this pre-selected y_0 moves the curve closer to the data points as shown in the Fig. 2 from the main text. However, this provides a worse fit than the linear fit strategy where the total absolute error is 936 MHz, instead of 293 MHz for the first six data points.

In conclusion, the measured data points can not be modeled using only a cubic function. A linear trend is observable at lower temperatures. Checking the goodness of fit values reveals 16 K as a suitable cutoff for determining the trend moving from linear to cubic.

S4. CPT MODELLING AND ANALYSIS

A. Lindblad Model for CPT Dynamics

In order to model the CPT dip, the evolution of three levels in a lambda scheme is calculated by numerically solving a Lindbladian master equation [6]:

$$\dot{\rho} = -\frac{i}{\hbar}[H, \rho] + \sum_{ij} \left(S_{ij} \rho S_{ij}^\dagger - \frac{1}{2} \{ S_{ij}^\dagger S_{ij}, \rho \} \right). \quad (3)$$

Here ρ is the density matrix given by $|\Psi\rangle\langle\Psi|$, where $|\Psi_0\rangle = 1|1\rangle + 0|2\rangle + 0|3\rangle$ is the initial state wavefunction. H is the coherent part of the equation and is given by:

$$H = \hbar \begin{bmatrix} 0 & 0 & \Omega_C/2 \\ 0 & \Delta_C - \Delta_D & \Omega_D/2 \\ \Omega_C/2 & \Omega_D/2 & \Delta_C \end{bmatrix}, \quad (4)$$

$$|\Psi\rangle = \alpha|B\rangle + \beta|D\rangle \quad (5)$$

where the matrix includes the Rabi frequencies Ω on both transitions (C, D) and the detunings Δ of the electromagnetic field. The S_{ij} terms in Eq. (3) are operators presenting the incoherent part of the equation and are given by Eq. (6), where i and j give the initial and final states respectively:

$$S_{ij} = \sqrt{\gamma_{ij}} |j\rangle\langle i|. \quad (6)$$

These matrix elements are identified with the following processes:

transitions between the ground-state orbital levels	$\gamma_{12} = \gamma_+$; $\gamma_{21} = \gamma_-$;
decays from the excited state	$\gamma_{31} = \gamma_C$; $\gamma_{32} = \gamma_D$;
and dephasing between the ground-state levels	$\gamma_{22} = \gamma_d$.

In order to fit the data, Eq. (3) is integrated until the steady state is achieved. In this work, 1 μ s turned out to be sufficient as the integration upper bound. This follows the fact that the state evolutions are dominated by γ_- that is in the order of few tens of picoseconds.

B. Fit Parameter Analysis

In Fig. S9, three different parameters (with subscripts 0) that are extracted from the fits from measurement number 17 (appendix A of the main text) are varied. As these three parameters have qualitatively different effects on the dip, one can treat them independently and implement a fitting algorithm.

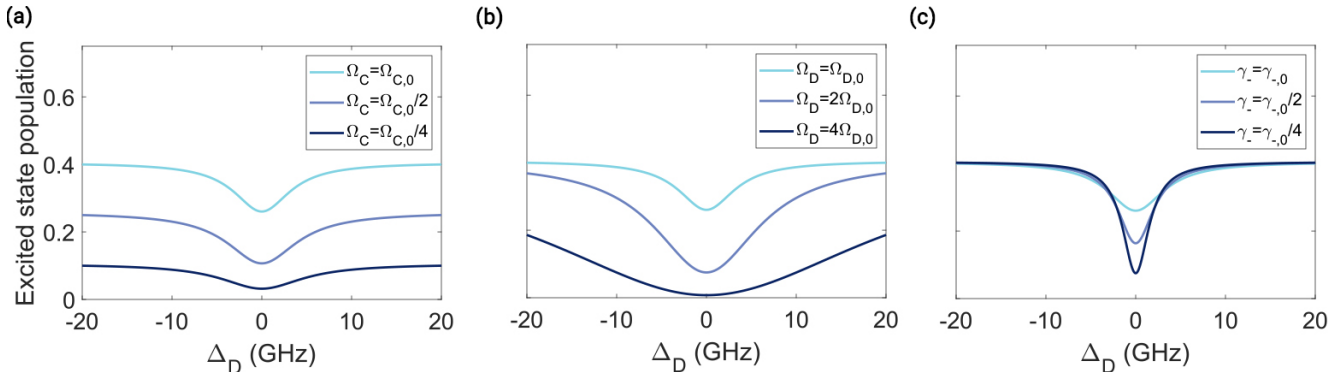


FIG. S9. Changes in the CPT dips as fit parameters (with subscripts 0) are varied. Different parameters affect the dip in different ways enabling the implementation of a fitting algorithm with multiple free parameters. (a) CPT dip as the Rabi frequency on the C transition is varied. Change of this parameter mainly determines the excited state population when D is highly detuned. (b) CPT dip as the Rabi frequency on the D transition is varied. Change of this parameter influences both the width and the depth of the dip. (c) CPT dip as the orbital phononic transition rates (both γ_+ and γ_- via thermalization) are varied. Changing this parameter only influences the depth of the dip.

C. CPT Analysis Steps

1. The frequencies are scanned between 30 to 200 times (on both directions), depending on the measurement and observed signal.
2. The frequency scans with the D laser is done via feeding an external voltage signal. As the scan continues, frequency of the laser is recorded through a pick-off. The extracted (voltage, signal) data points are changed into (frequency, signal) by correlating the time stamps of the voltages and frequencies.
3. All the scans in a measurement are binned according to one of the frequency arrays.
4. All the bins that have more than 2 kc/s are averaged. The data points with under 2 kc/s are neglected, as the drop in counts indicate measurements where a spectral jump has occurred and the signal is temporarily diminished.
5. A pre-fit using a Gaussian function is applied to determine the center of the dip, and the averaged and centered fluorescence data are extracted.
6. Using the saturation measurement, the fluorescence signal is scaled to a population where the excited state is assumed to be 50% at saturation.
7. $\gamma_C + \gamma_D$ is extracted from the lifetime measurement, and their branching (2.4:1) is determined from the PL spectrum.
8. A second level fit is applied using a numerical black box optimization function in Wolfram Mathematica (NMinimize), where an error function defined by the sum of $|x_{i,\text{experimental}} - x_{i,\text{model}}|^2$ at each data point, i , is minimized by changing the Ω_C , Ω_D and γ_- parameters, where $\gamma_+ = \gamma_- \exp\left[-\frac{\hbar\Delta_{12}}{k_B T}\right]$. k_B is the Boltzmann constant, $\Delta_{12} = 831$ GHz is the ground state splitting extracted from the resonances identified during a CPT measurement, and $T = 3.86$ K is the temperature.
9. To estimate the fitting sensitivity, each fit parameter is changed on both directions, and the CPT dip population at two-photon resonance is monitored. The maximal value from both directions that changes the dip by more than 5% is selected as the uncertainty.

D. All CPT Measurements

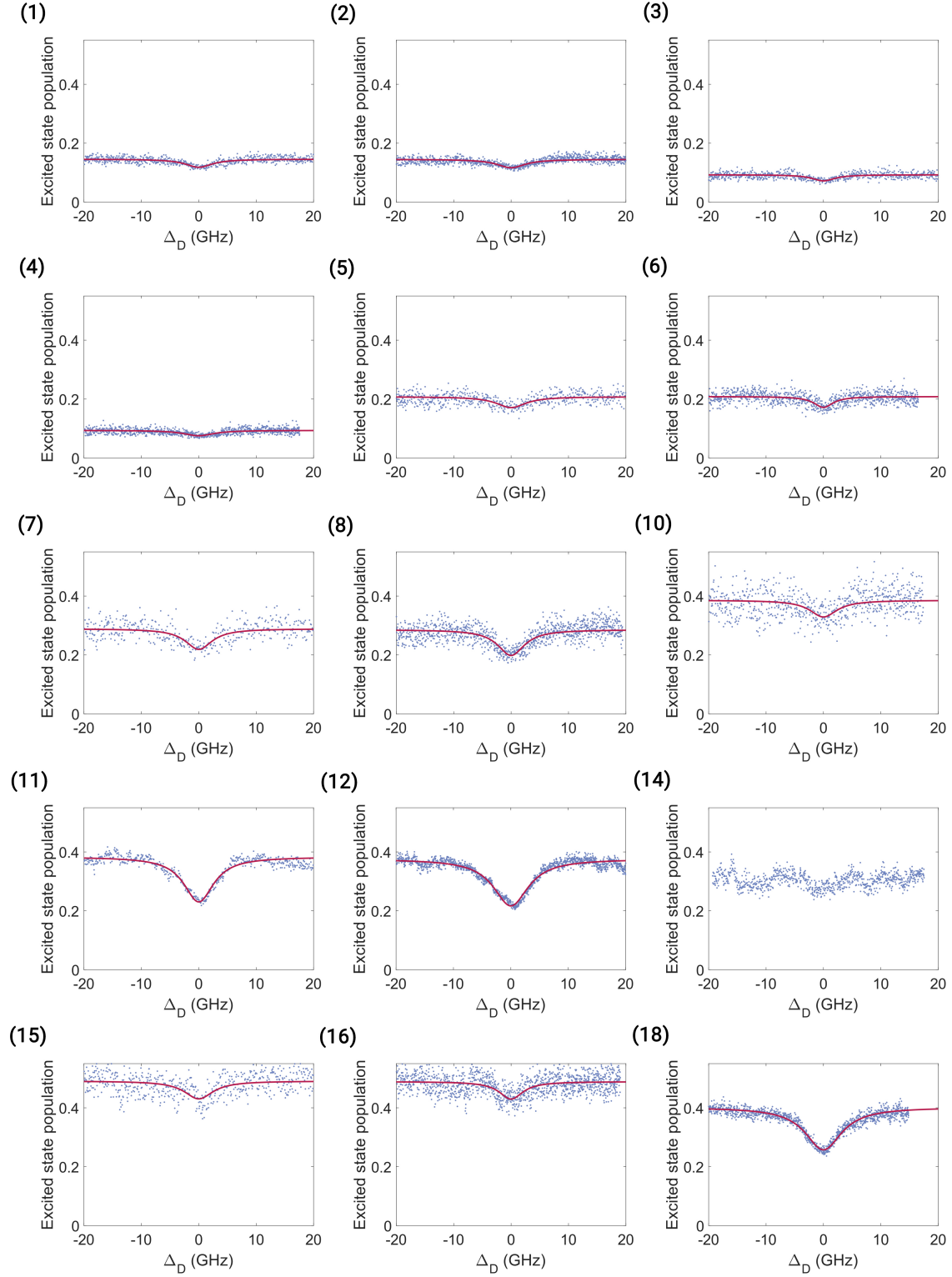


FIG. S10. All the analyzed CPT data and their fits (solid line) based on the model presented in supplementary section S4 A. The measurement parameters and the extracted values are provided in the main text appendix A with the measurement indices.

S5. PHONONIC BROADENING OF THE D TRANSITION AT 4K

In this section, an overview of the phononic relaxation time scale estimated from the linewidth of the D transition γ_D presented in Fig. 4 from the main text, using the analysis provided in [7] is provided.

The homogeneous linewidth of the C (D) transition $\Gamma_{C(D),\text{hom}}$ is calculated from the lifetime τ_{se} presented in Fig. S6 and the photoluminescence spectrum peak ratio presented in Fig. S4 for estimate the individual emission lifetimes:

$$\Gamma_{D,\text{hom}} = 1/(2\pi\tau_{\text{se}} * 1/3.4) \quad (7)$$

$$\Gamma_{C,\text{hom}} = 1/(2\pi\tau_{\text{se}} * 2.4/3.4) \quad (8)$$

The same peak ratios are used to estimate the D transition saturation power $P_{\text{sat},D}$ from the C transition saturation power P_{sat} presented in Fig. S7:

$$P_{\text{sat},D} = P_{\text{sat}} * 2.4 \quad (9)$$

From these values, the power broadening components for the C (D) transition $\Gamma_{C(D),\text{pow}}$ are calculated:

$$\Gamma_{C,\text{pow}} = \Gamma_{C,\text{hom}}\sqrt{1 + P_C/P_{\text{sat}}} - \Gamma_{C,\text{hom}} \quad (10)$$

$$\Gamma_{D,\text{pow}} = \Gamma_{D,\text{hom}}\sqrt{1 + P_D/P_{\text{sat},D}} - \Gamma_{D,\text{hom}} \quad (11)$$

From the measured C transition linewidth Γ_C presented in Fig. S5, the spectral diffusion component for both transitions Γ_{diff} is estimated by:

$$\Gamma_{\text{diff}} = \Gamma_C - \Gamma_{C,\text{hom}} - \Gamma_{C,\text{pow}} \quad (12)$$

This method, however, assumes the D transition couples to the external charge noise exactly the same as the C transition [8, 9], therefore should only be treated as an estimation.

Finally, by subtracting all the remaining components, we extract phononic broadening component $\Gamma_{D,\text{phon}}$ of the D transition linewidth:

$$\Gamma_{D,\text{phon}} = \Gamma_D - \Gamma_{D,\text{hom}} - \Gamma_{D,\text{pow}} - \Gamma_{\text{diff}} \quad (13)$$

T_- depends on the $\Gamma_{D,\text{phon}}$ by a Fourier transform relation:

$$T_- = 1/(2\pi\Gamma_{D,\text{phon}}) \quad (14)$$

-
- [1] K. J. Brown, E. Chartier, E. M. Sweet, D. A. Hopper, and L. C. Bassett, Cleaning diamond surfaces using boiling acid treatment in a standard laboratory chemical hood, *J. Chem. Heal. Saf.* **26**, 40 (2019).
 - [2] H. A. Atikian, A. Eftekharian, A. Jafari Salim, M. J. Burek, J. T. Choy, A. Hamed Majedi, and M. Lončar, Superconducting nanowire single photon detector on diamond, *Appl. Phys. Lett.* **104**, 122602 (2014).
 - [3] J. F. Ziegler, M. D. Ziegler, and J. P. Biersack, SRIM – The stopping and range of ions in matter, *Nuclear Instruments and Methods in Physics Research Section B: Beam Interactions with Materials and Atoms* **268**, 1818 (2010).
 - [4] J. M. Binder, A. Stark, N. Tomek, J. Scheuer, F. Frank, K. D. Jahnke, C. Müller, S. Schmitt, M. H. Metsch, T. Uden, T. Gehring, A. Huck, U. L. Andersen, L. J. Rogers, and F. Jelezko, Qudi: A modular python suite for experiment control and data processing, *SoftwareX* **6**, 85 (2017), 1611.09146.
 - [5] S. C. Kitson, P. Jonsson, J. G. Rarity, and P. R. Tapster, Intensity fluctuation spectroscopy of small numbers of dye molecules in a microcavity, *Physical Review A* **58**, 620 (1998).
 - [6] D. Manzano, A short introduction to the Lindblad master equation, *AIP Advances* **10**, 025106 (2020).
 - [7] P. Wang, L. Kazak, K. Senkalla, P. Siyushev, R. Abe, T. Taniguchi, S. Onoda, H. Kato, T. Makino, M. Hatano, F. Jelezko, and T. Iwasaki, Transform-Limited Photon Emission From a Lead-Vacancy Center in Diamond Above 10 K, *arXiv preprint*, 2308.00995 (2023).
 - [8] L. de Santis, M. E. Trusheim, K. C. Chen, and D. R. Englund, Investigation of the Stark Effect on a Centrosymmetric Quantum Emitter in Diamond, *Physical Review Letters* **127**, 147402 (2021).
 - [9] S. Aghaeimeibodi, D. Riedel, A. E. Rugar, C. Dory, and J. Vučković, Electrical Tuning of Tin-Vacancy Centers in Diamond, *Physical Review Applied* **15**, 064010 (2021).